

Liquid crystalline growth within a phase-field crystal model

Sai Tang,^{1,2} Simon Praetorius,² Rainer Backofen,² Axel Voigt,^{2,3} Yan-Mei Yu,⁴ and Jincheng Wang¹

¹*State Key Laboratory of Solidification Processing,*

Northwestern Polytechnical University, Youyi Western Road 127, 710072 Xi'an, China

²*Institut für Wissenschaftliches Rechnen, Technische Universität Dresden, 01062 Dresden, Germany*

³*Center of Advanced Modeling and Simulations, Technische Universität Dresden, 01062 Dresden, Germany*

⁴*Institute of Physics, Chinese Academy of Science, P. O. Box 603, 100190 Beijing, China*

By using a phase-field crystal (PFC) model, the liquid-crystal growth of the plastic triangular phase is simulated with emphasis on crystal shape and topological defect formation. The equilibrium shape of a plastic triangular crystal (PTC) grown from an isotropic phase is compared with that grown from a columnar/smectic A (CSA) phase. While the shape of a PTC nucleus in the isotropic phase is almost identical to that of a classical PFC model, the shape of a PTC nucleus in CSA is affected by the orientation of stripes in the CSA phase, and irregular hexagonal, elliptical, octagonal, and rectangular shapes are obtained. Concerning the dynamics of the growth process we analyse the topological structure of the nematic-order, which starts from nucleation of $+\frac{1}{2}$ and $-\frac{1}{2}$ disclination pairs at the PTC growth front and evolves into hexagonal cells consisting of $+1$ vortices surrounded by six satellite $-\frac{1}{2}$ disclinations. It is found that the orientational and the positional order do not evolve simultaneously, the orientational order evolves behind the positional order, leading to a large transition zone, which can span over several lattice spacings.

PACS numbers: 68.08.De, 61.30.Dk, 64.70.D, 82.70.Dd

I. INTRODUCTION

Phase field crystal (PFC) models, introduced by Elder et al. [1, 2] are today widely used in modeling of crystallization, e.g. [3–7]. As a mean-field approach, the PFC model is capable to describe, over diffusive time scales, atomic arrangements, crystalline defects and interface structures of the crystal growth process. The modeling approach has also been generalized to other systems, e.g. liquid crystals. Liquid crystal PFC (LC-PFC) models [8] are formulated in terms of three order parameter fields including the reduced translational density $\psi(\vec{r}, t)$, the local nematic order parameter $S(\vec{r}, t)$, and the mean nematic director $\hat{n}(\vec{r}, t)$, wherein $\vec{r} = (x, y)$ and t are position and time, respectively. The couplings among these fields in two dimensions produce the liquid crystalline phases, such as isotropic, nematic, columnar/smectic-A, and plastic crystalline phases (a meso-phase which presents ordered translational density field with crystalline symmetry and macroscopically disordered orientation field [9–13]). Achim et al. [14] numerically determined the stable liquid-crystalline phases and Praetorius et al. [15] found the corresponding phase coexistence regions for special coupling-parameter combinations. The latter group also explored the structure and width of the equilibrium PTC-isotropic and PTC-CSA interface as a function of model parameters related to the coupling strength of the three fields and crystal anisotropy.

We here extend these studies to investigate the growth of a PTC nucleus from the isotropic and the CSA phase. Experimental results [16, 17] have shown such growth processes to produce a large variety of shapes, e.g. with smooth or faceted dendrites, faceted equilibrium shapes or circular shapes. The growth of Succinonitrile and Pivalic acid [16] from melt e.g. show high similarity with

metal systems in terms of the observed morphologies. This suggests that for some plastic materials the coupling strength of the translational and orientational field may have only limited influence on the morphology. Is this specific to these materials or can the coupling strength also play an important role in the shape evolution of plastic crystal growth? Besides the morphology we will also consider topological defects of the nematic director $\hat{n}(\vec{r})$. They have already been considered e.g. in [14, 18–20]. Achim et al. [14] obtained vortices, disclinations, sources or sinks, and hyperbolic points in PTC. Cremer et al. [20] depicted the topological defect structure in PTC, and proposed a simplified but topologically equivalent model to explain qualitatively how the topological defect structure of hexagonal symmetry arises. Nevertheless, the understanding about the process of topological defect formation is still limited. How does the topological defect originate from the mother phase? How is a topological defect structure of geometric symmetry constructed? We will answer these questions by visualizing the topological defect formation on particle scale using the LC-PFC model.

II. LIQUID CRYSTAL PFC MODEL

A. Free-energy functional

We consider a formulation of the LC-PFC model using the reduced translational density field $\psi(\vec{r}, t)$, and the symmetric and traceless nematic order tensor fields $Q_{ij}(\vec{r}, t)$. In two dimensions the $Q_{ij}(\vec{r}, t)$ fields are related to the nematic order parameter $S(\vec{r}, t)$ and the nematic

director $\hat{n}(\vec{r}, t) = (n_1, n_2)$ fields through

$$Q_{ij}(\vec{r}, t) = S(\vec{r}, t) \left(n_i(\vec{r}, t) n_j(\vec{r}, t) - \frac{1}{2} \delta_{ij} \right). \quad (1)$$

Thus, the nematic order parameter $S(\vec{r}, t)$ and nematic director $\hat{n}(\vec{r}, t)$ can be obtained from the nematic order tensor $Q_{ij}(\vec{r}, t)$. The dimensionless free energy-functional is written as [8, 14, 15],

$$\begin{aligned} \mathcal{F}[\psi, Q_{ij}] = \int d^2r \left(-\frac{\psi^3}{3} + \frac{\psi^4}{6} + (\psi - 1) \frac{\psi Q_{kl}^2}{4} \right. \\ \left. + \frac{Q_{kl}^2 Q_{mn}^2}{64} + A_1 \psi^2 + A_2 \psi (\Delta + \Delta^2) \psi \right. \\ \left. + B_3 (\partial_k \psi) (\partial_l Q_{kl}) + D_1 Q_{kl}^2 + D_2 (\partial_l Q_{kl})^2 \right), \end{aligned} \quad (2)$$

where, Einsteins's sum convention is used, $\Delta \equiv \partial_k^2$ is the Laplace operator, and $A_1, A_2, B_3, D_1,$ and D_2 are dimensionless model parameters, with A_1 controlling the crystalline anisotropy and B_3 the coupling strength between $\psi(\vec{r}, t)$ and $Q_{ij}(\vec{r}, t)$.

B. Dynamic equations

The dynamic equations of $\psi(\vec{r}, t)$ and $Q_{ij}(\vec{r}, t)$ are deduced from classical dynamical density functional theory (DDFT), as written by [21, 22],

$$\dot{\psi} + \partial_i J_i^\psi = 0, \quad (3)$$

$$\dot{Q}_{ij} + \Phi_{ij}^Q = 0, \quad (4)$$

where $J_i^\psi(\vec{r}, t)$ is the dimensionless current and $\Phi_{ij}^Q(\vec{r}, t)$ is the dimensionless quasi-current. In constant-mobility approximation, this current and quasi-current are given by [3]

$$J_i^\psi = -2\alpha_1 (\partial_i \psi^\natural) - 2\alpha_3 (\partial_j Q_{ij}^\natural), \quad (5)$$

$$\begin{aligned} \Phi_{ij}^Q = -4\alpha_1 (\Delta Q_{ij}^\natural) - 2\alpha_3 (2(\partial_i \partial_j \psi^\natural) - \delta_{ij} (\Delta \psi^\natural)) \\ + 8\alpha_4 Q_{ij}^\natural, \end{aligned} \quad (6)$$

where $\alpha_1, \alpha_3,$ and α_4 are dimensionless mobilities. The thermodynamic conjugates ψ^\natural and Q_{ij}^\natural are given by

$$\psi^\natural = \frac{\delta \mathcal{F}}{\delta \psi}, \quad Q_{ij}^\natural = \frac{\delta \mathcal{F}}{\delta Q_{ij}}, \quad (7)$$

which read

$$\begin{aligned} \psi^\natural = -\psi^2 + \frac{2}{3} \psi^3 + (2\psi - 1) \frac{Q_{ij}^2}{4} + 2A_1 \psi \\ + 2A_2 (\Delta + \Delta^2) \psi - B_3 (\partial_i \partial_j Q_{ij}), \end{aligned} \quad (8)$$

$$\begin{aligned} Q_{ij}^\natural = \psi(\psi - 1) Q_{ij} + \frac{Q_{ij} Q_{kl}^2}{8} \\ - B_3 (2(\partial_i \partial_j \psi) - \delta_{ij} \Delta \psi) + 4D_1 Q_{ij} \\ - 2D_2 \partial_k (\partial_i Q_{kj} + \partial_j Q_{ki} - \delta_{ij} (\partial_l Q_{kl})). \end{aligned} \quad (9)$$

The dynamic equations (3) and (4) will be solved numerically by a semi-implicit Fourier method, see appendix A for details.

III. RESULTS AND DISCUSSION

We consider first a PTC nucleus in the isotropic and CSA phase and show that the coupling strength between the nematic order tensor and the density, B_3 , has only a minor influence on the crystal morphology. Secondly, the ordering of the nematic order tensor during growth of a PTC into the CSA phase is studied. Independent on the coupling strength, B_3 , $+1$ disclinations in the PTC phase are formed by coalescence of two $+\frac{1}{2}$ disclinations. Only the time evolution and the delay of the defect formation with respect to the interface velocity is dependent on B_3 .

A. Stationary Interfaces

All simulations are carried out with $A_2 = 14, D_1 = 1$ and $D_2 = 0.8$. Variations of these parameters turn out

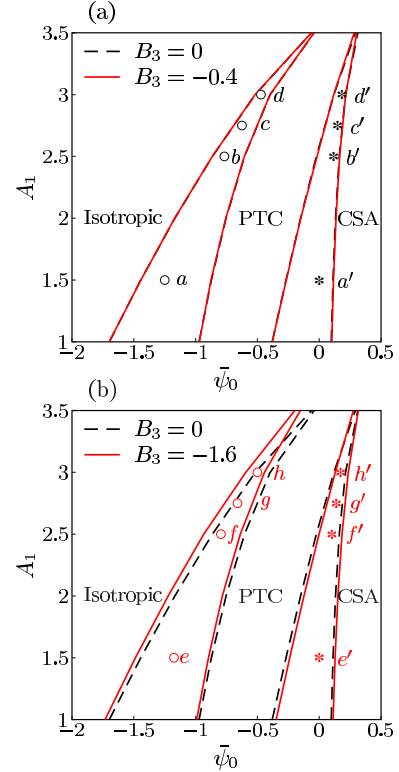


FIG. 1. LC-PFC phase diagrams as function of $\bar{\psi}_0$ and A_1 for $B_3 = 0, -0.4$ (a), and -1.6 (b) that correspond to zero, weak, and strong coupling strength between the density field and the nematic-order field, respectively. The small letters correspond to parameters used in our simulations below.

to show only minor effects on the considered situation of isotropic, PTC and CSA phases. We vary the mean den-

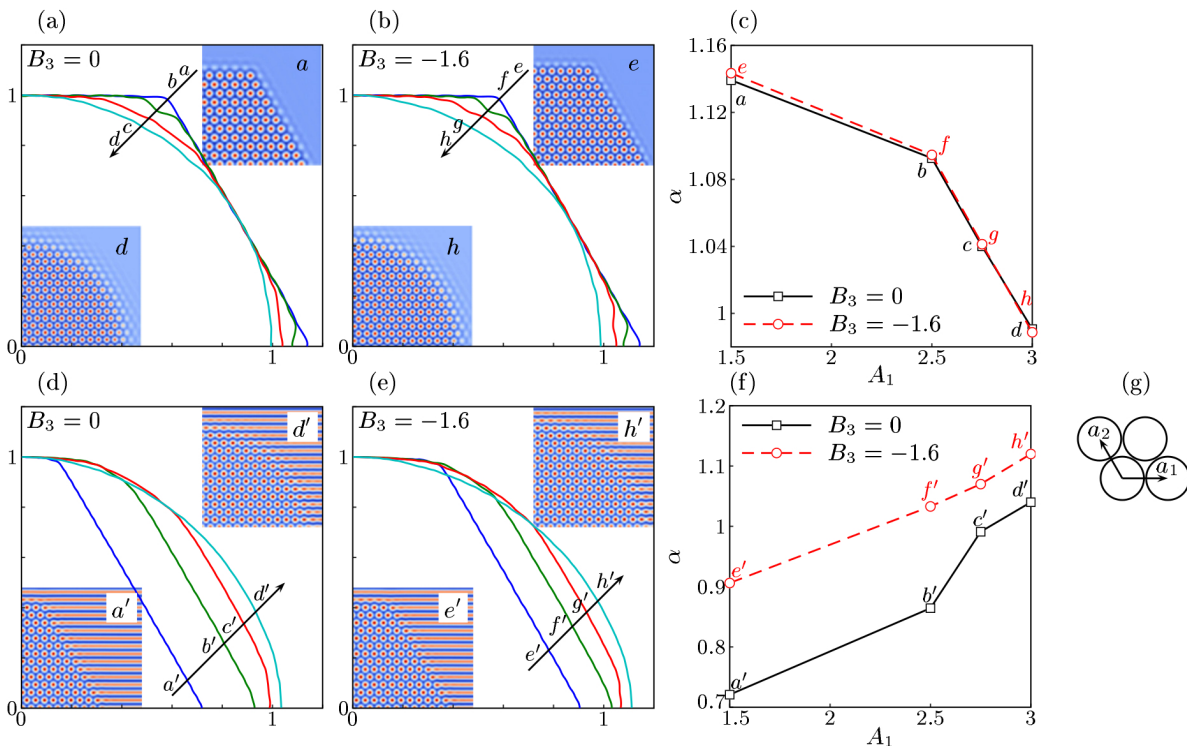


FIG. 2. The equilibrium shape of the PTC nucleus in the isotropic phase (top) for $B_3 = 0$ (a) and $B_3 = -1.6$ (b) and the corresponding contour line and aspect ratio α as a function of A_1 in (c). The considered examples a-d and e-h correspond to the depicted points in Fig. 1. The inlets show the obtained equilibrium shapes for two selected points. The morphology of a PTC nucleus in a CSA phase (bottom) for $A_1 = 1.5$, where the close-packed direction of the PTC phase is parallel to the stripe in the CSA phase. (d) show the equilibrium PTC shapes for $B_3 = 0$ for the considered examples a'-d', (e) shows the shapes of growing PTC for $B_3 = -1.6$ for h'-e', again corresponding to the depicted points in Fig. 1. The inlets again show selected growth shapes. (f) shows the aspect ratio α as a function of A_1 for the equilibrium PTC shape for $B_3 = 0$ and the growing shape for $B_3 = -1.6$. (g) shows the definition of crystal unit vectors a_1 and a_2 .

sity $\bar{\psi}_0$, anisotropy A_1 and coupling strength B_3 , which can be used to control the liquid crystal phases [14, 15].

In Fig. 1, the phase diagram without coupling to the nematic tensor, $B_3 = 0$, is compared to the phase diagrams with weak and strong coupling, $B_3 = -0.4$ resp. -1.6 . The structure of the phase diagrams reflect that of the classical PFC, where the PTC and the CSA phase correspond to the crystal and stripe phase, cf. [1]. Thus, analog to the classical PFC A_1 is connected to the undercooling. The coupling strength does not change the phase diagram qualitatively. Small coupling, $B_3 = -0.4$, shows no influence, only strong coupling, $B_3 = -1.6$, slightly increases the region of a stable PTC phase. Thus, the coexistence region of a PTC-isotropic and a PTC-CSA phase is nearly independent on B_3 and allows us to study the interface properties dependent on coupling strength, B_3 , only. In order to minimize boundary effects in our simulations, a single PTC nucleus is considered in the center of the simulation domain. To neglect induced stresses by the boundaries, the parameters A_1 and B_3 are varied and the corresponding $\bar{\psi}_0$ value is chosen carefully to assure coexistence with the surrounding phase, cf. [15]. As long as we are in the coexistence region of the phase diagram, variations

in $\bar{\psi}_0$ do not change the morphology but determines the size of the PTC nucleus. Size dependence for very small nuclei, as observed in [23] can here be neglected as only large enough PTC crystals are considered. The domain size is at least 2 times bigger than the shown PTC crystal for the coexistence with the CSA phase and possible size dependencies are regularly checked by enlarging the simulation box and comparing the results.

1. Equilibrium shape of PTC in isotropic phase

The equilibrium shape of a PTC nucleus in the isotropic phase is simulated for increasing A_1 . Simulation results and parameters are summarized in Fig. 2 (a)-(c). For every equilibrium shape the interface has been extracted and normalized by the extension of the PTC nucleus in [12]-direction. Without coupling, $B_3 = 0$, the shape changes from a perfect hexagon, $A_1 = 1.5$, to a circle, $A_1 = 3$. The width of the interface seen in the inlet of Fig. 2 (a) widens for increasing A_1 . This corresponds to the findings in classical PFC for decreasing undercooling, cf. [23]. Coupling to the nematic tensor does not change the picture at all, see Fig. 2 (b). The anisotropy of the nu-

cleus is quantified by the reduced aspect ratio α (ratio of the nucleus extension in [10]- and [12]-direction). Based on the Wulff construction, the aspect ratio α relates to the anisotropy of the line energy [23, 24]. Thus, the nematic order has minor influence on the anisotropy of the line energy of the PTC phase in the isotropic phase and the anisotropy is well controlled by A_1 only and reflects the results of classical PFC [23].

2. Crystal shape of PTC in CSA phase

For PTC growth in the CSA phase, the orientation of the nucleus with respect to the stripes of the CSA phase becomes important. We consider two set ups. Firstly, the [12]-direction of the PTC crystal is perpendicular to the stripes. That is, closed packed layers of the crystal and stripes of the CSA phase are aligned perfectly (case I). Secondly, the crystal is rotated by $\frac{\pi}{2}$ and the stripes do not fit the particle layers (case II).

The simulation results for case I are shown in Fig. 2 (d)-(f). As before, the growth of a small PTC nucleus is simulated until a steady state is reached. The anisotropy of the steady state is again controlled by A_1 . Increasing A_1 changes the morphology from faceted to round, Fig. 2 (d). But the round shapes are here elongated along the stripes, while the faceted shapes are elongated perpendicular to the stripes. Unlike growth into the isotropic phase, the growth kinetics is very anisotropic for small A_1 . That is, the growth of the crystal facet in [12]-direction is faster than the growth of the [21]-facet. This leads to a smaller [12]-facet compared to the [21]-facet of the stationary crystal. The ratio of the length of two facets is dependent on initial condition and domain size of the simulation. Thus, they are just metastable or frozen states and do not represent the overall anisotropy of the interface energy. But, as there has been always facets, we can conclude that the line energy has strong minima for [12]- and [21]-facets, but we cannot judge the energy ratio between them.

Increasing the coupling strength, B_3 , the transition from faceted to round shapes does not change, but the elongation of the round shapes along the stripes is slightly increased, see Fig. 2 (e). The coupling strength in this situation is more important than for the PTC-isotropic interface.

In case II, the crystal is rotated and the simulations are done as before. The PTC crystal does not fit anymore into the layers of the CSA phase, see Fig. 3. In this configuration only small crystals for small A_1 could be stabilized. Various attempts to increase nucleus sizes lead to rotating or vanishing crystals. The [10]-plane of the PTC crystal is parallel to the stripes and stabilized by the CSA phase. This leads roughly to a hexagon with the edges in [10]-direction cut. The CSA phase is also distorted near the interface. If the stripes do not fit to the structure of the PTC crystal, the crystal and the CSA phase is inhomogeneously strained. This is clearly shown by the bend-

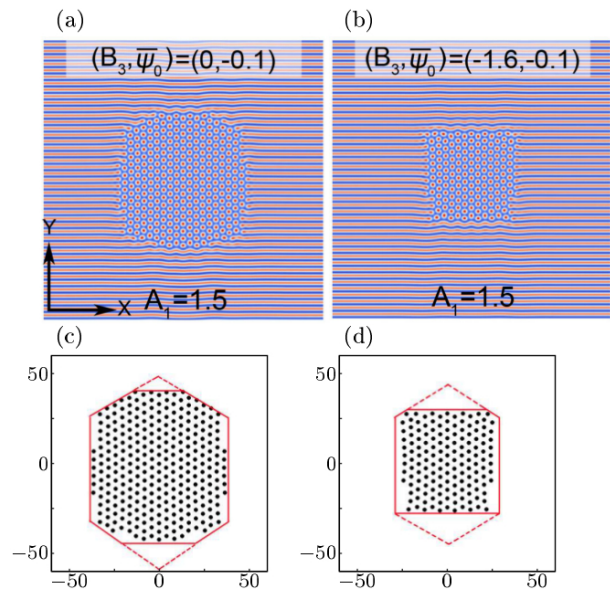


FIG. 3. The PTC shape in the CSA phase for $A_1 = 1.5$, $B_3 = 0$ (a) and (c) and $B_3 = -1.6$ (b) and (d), where the closed packed crystal direction is perpendicular to the stripe in the CSA phase. (c) and (d) show a sketch of the PTC shape in CSA phase.

ing of the closed packed particle layers in Fig. 3 (b) and the waviness of the stripes in the CSA phase. The coupling strength increases the discussed features and lead to nearly rectangular shapes, Fig. 3 (b,d). Thus, case II is energetically penalized by the elastic stress in the crystal induced by the surrounding CSA phase and will most likely not occur in liquid crystal phase transition. In the following we will concentrate on case I.

B. Topological defect formation

The PTC phase exhibits not only the characteristics of the crystalline phase, but also shows nematic ordering with topological defects. Here we examine, how the nematic ordering evolves at the PTC-isotropic and the PTC-CSA interface. The simulations are set up as above. But we restrict ourselves to the interface in the regime of constant growth velocity. Fig. 4 shows the nematic order parameter $S(\vec{r})$ and director $\hat{n}(\vec{r})$ at the [12]-interface. In the PTC phase along the shown direction, $+1$ vortices and pairs of $-\frac{1}{2}$ disclinations alternate [14]. Towards the isotropic phase the nematic order parameter not only decreases, but also the structure of the ordering changes, see Fig. 4 (a) and (c) and for details Fig. 5. The $+1$ vortex splits in two $+\frac{1}{2}$ disclinations. This disclination pair increases its distance and finally vanishes as the nematic ordering vanishes. Growth towards the CSA phase, changes the situation only a little, Fig. 4 (b) and (d). The PTC and CSA phase show different nematic ordering, but the splitting of $+1$ vortices is also observed. Furthermore, in the PTC isotropic growth the nematic order

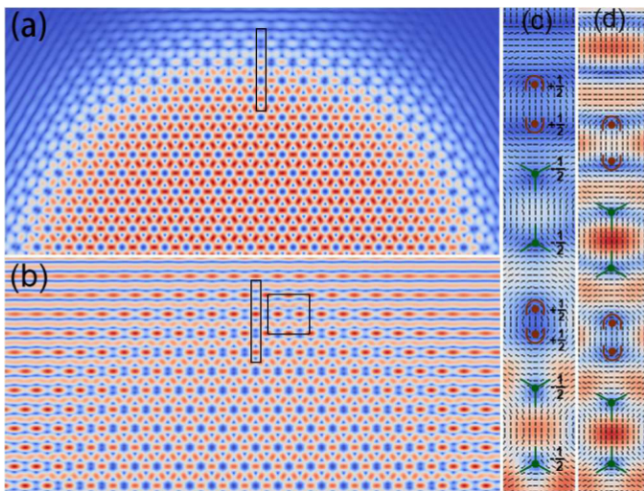


FIG. 4. The topological structure of the PTC phase grown from the isotropic phase (a) and the CSA phase (b). The magnified view of area denoted by black boxes in (a) and (b) is given in (c) and (d), respectively, where the short arrows represent the director field of the topological structure.

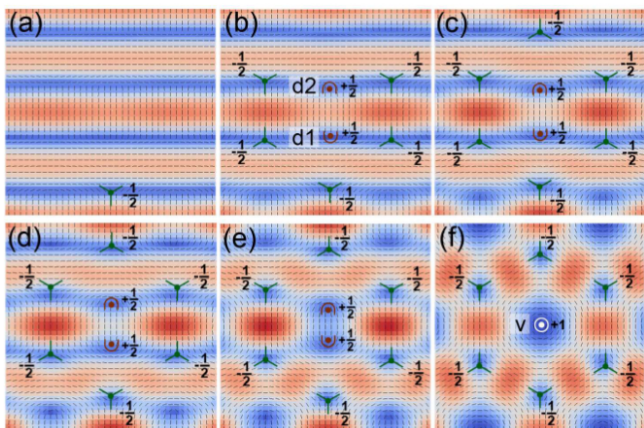


FIG. 5. The snapshots of the topological defect structure formation in the region enclosed by square box in Fig. 4 (b) during the PTC growth in the CSA phase. d1 and d2 are a pair of $+\frac{1}{2}$ disclinations. The PTC-CSA interface moves from bottom to top from (a) to (f), and for (d) and (e) the region around d1 and d2 is locating inside the PTC-CSA interface.

parameter forms a weak columnar structure ahead of the growth front. Thus, the PTC isotropic phase transition has an intermediate stripe phase. The structure of the topological defects of the nematic director $\hat{n}(\vec{r}, t)$ at the PTC growth front are similar for both cases.

Fig. 5 shows the formation process of the topological defect structure of the PTC phase grown towards the CSA phase. Firstly, fluctuation in the $\hat{n}(\vec{r}, t)$ field and nematic order parameter field $S(\vec{r}, t)$ arises up at the PTC growth front. This leads to $+\frac{1}{2}$ and $-\frac{1}{2}$ disclination pairs, Fig. 5 (a) and (b). Next, two $+\frac{1}{2}$ disclinations approach each other gradually and coalesce into a $+1$ vortex,

Fig. 5 (c) and (e). The $-\frac{1}{2}$ disclinations do not move. At the end, a basic unit, the $+1$ vortex surrounded by six $-\frac{1}{2}$ disclinations is formed, Fig. 5 (f). This constitutes the topological defect structure in the bulk PTC phase. It was found that the coalescence of two disclinations with the same charge is energetically unfavored [25]. Nevertheless, during PTC growth, the advancing interface drives coalescence of two $+\frac{1}{2}$ disclinations. In the following, the kinetics of this topological defects formation will be discussed in more detail. Firstly, we study the growth

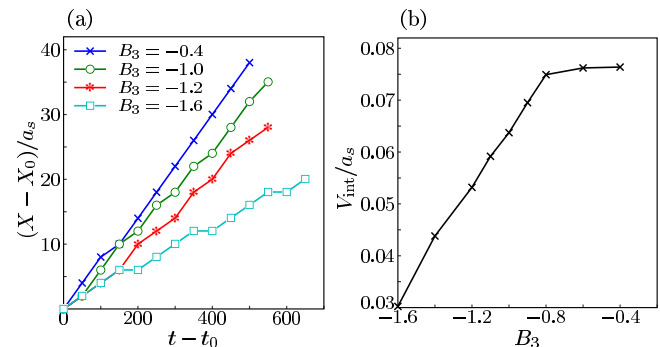


FIG. 6. The growth kinetics of PTC-CSA interface. The displacement of PTC-CSA interface versus time t (a), and growth velocity (b) for various B_3 . X is the position of PTC-CSA interface at different times, and X_0 the initial position at time t_0 .

velocity of the PTC nucleus from the CSA phase along the direction normal to stripes as shown in Fig. 4 (b). After some initial relaxation the displacement of the PTC-CSA interface increases linearly with time and a constant growth velocity, V_{int} , is achieved, Fig. 6 (a). The dependence of the growth velocity on the coupling strength B_3 is shown in Fig. 6 (b). A strong and weak coupling regime can be identified. For strong coupling, the growth velocity increases linearly with B_3 , changing from -1.6 to -0.8 . For weak coupling, when B_3 is in the range between -0.8 and -0.4 , the growth velocity shows little dependence on B_3 . Starting from the growth velocity V_{int} , the defect moving velocity V_d is scaled as $\tilde{V} = V_d/V_{int}$, and time t is scaled as $\tilde{t} = t/(a_s/V_{int})$, with the lattice constant of the CSA phase $a_s = 2\pi/\sqrt{1/2} \approx 8.8858$. This can be used to count the number of lattices in the CSA phase that the PTC-CSA interface has advanced. The coalescence of two $+\frac{1}{2}$ disclinations is illustrated in Fig. 7 in more detail. The position of the topological defects are easily identified at the minima of the nematic order parameter $S(\vec{r}, t)$, Fig. 7 (a). Initially, there are two minima in $S(\vec{r}, t)$ profiles which correspond to the disclinations d1 and d2, respectively. The two minima approach gradually and coalesce finally at $\tilde{t} = 19.1$. To compare the evolution of the density field and the orientational field, we extract the density profile when the PTC-CSA interface is sweeping the region around d1 and d2 at $\tilde{t} = 12.5$. As shown in Fig. 7 (b), the peak value of the density profile at the position marked by the left red dash line almost equals

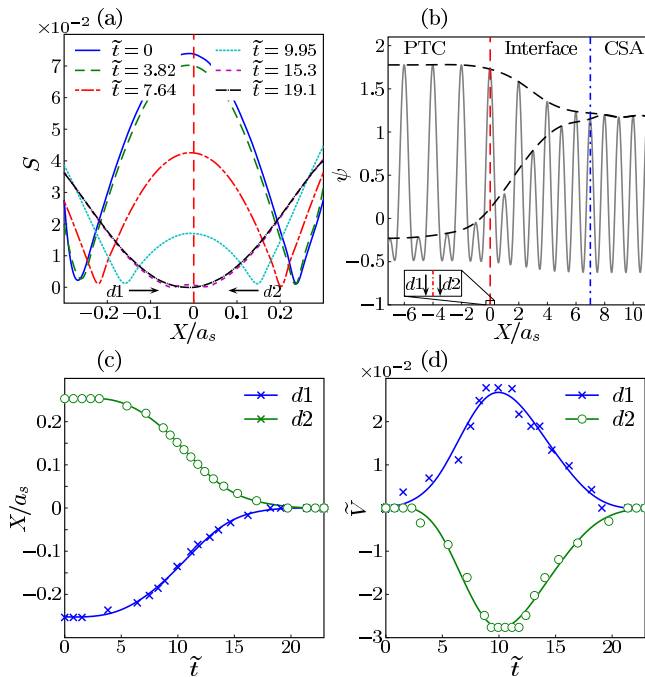


FIG. 7. The moving trajectory of two $+\frac{1}{2}$ disclinations d1 and d2, corresponding to Fig. 5, as represented by the $S(\vec{r}, t)$ profile (a), profile of density field corresponding to the $S(\vec{r}, t)$ when $t = 130$ (i.e., $\tilde{t} = 12.5$) (b), the position (c), and the velocity (d) of d1 and d2. Note that the red dashed line in (a) and (b) denotes the region in the vicinity of d1 and d2, and the region on the left side of the red dashed line in (b) is the PTC phase, the region on the right sides of the blue dash dotted line is the CSA phase, and the region between the two lines is the PTC-CSA interface (the left and the right boundary of the interface is determined by the criterion that the height of the peaks is lower than 0.95 of that in the bulk PTC phase and the CSA phase, respectively). The arrows in (a) denote the moving direction of d1 and d2.

that of the bulk PTC phase. However, the corresponding $S(\vec{r}, t)$ profile at the same time ($\tilde{t} = 12.5$) indicates that the evolution of the orientational field in the region around d1 and d2 is still far from being completed. The distance between d1 and d2 versus \tilde{t} is illustrated in Fig. 7 (c). We can see that d1 and d2 move nearly symmetrically. The velocities of d1 and d2 are given in Fig. 7 (d). The largest velocity occurs about the time $\tilde{t} = 12.5$. This corresponds to the moment when the growth front is sweeping the region around d1 and d2, which corresponds to the state in Fig. 5 (e), and when the density field evolution around d1 and d2 has almost completed, as shown in Fig. 7 (b). With the PTC-CSA interface approaching the region around d1 and d2, the velocities of d1 and d2 increase rapidly, while decrease steeply after the interface left away from them. In other words, the evolution of topological defect formation is accelerated by the advancing PTC-CSA interface. When the $+1$ vortex forms through the coalescence of d1 and d2, the interface has moved forward by a distance of about 20 lattice constants compared with the position when it

passes d1 and d2.

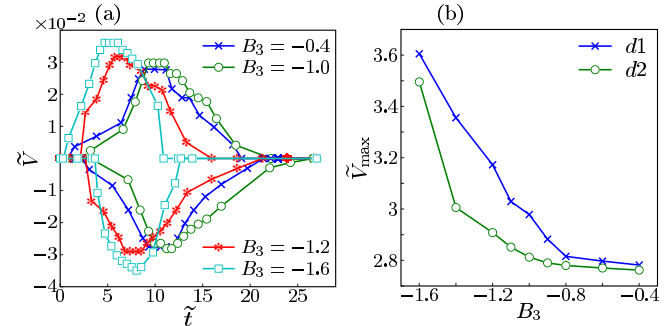


FIG. 8. The influences of coupling strength B_3 on topological defects formation kinetics: (a) the velocity of two $+\frac{1}{2}$ disclinations during the formation of $+1$ vortex for various B_3 , and (b) the peak value of the velocity curves as shown in (a) as a function of B_3 .

Finally, we investigated the influence of coupling strength on $+1$ vortex formation kinetics. As shown in Fig. 8 (a), with coupling strength increasing by decreasing B_3 from -0.4 to -1.6 , the peaks of velocity curves increase, and the scaled time \tilde{t} needed for the formation of a $+1$ vortex decreases. This indicates that the evolution from d1 and d2 to a $+1$ vortex can be completed faster for higher coupling strength. The dependence of peak velocities of the curves in Fig. 8 (a) on B_3 is summarized in Fig. 8 (b). For weak coupling strength when B_3 is between -0.8 and -0.4 , the peak velocities of d1 and d2 are nearly the same, and the motion of d1 and d2 are approximately symmetrical. However, with coupling strength increasing further ($B_3 < -1.0$), the peak velocities of d1 and d2 increase substantially, and d1, the disclination moving along the same direction as the PTC-CSA interface advances, has a larger peak velocity than that of d2, moving opposite to the PTC-CSA interface. Thus, it is shown that the increase of coupling strength accelerates the topological defect formation during PTC growth.

IV. CONCLUSION

In summary, by using the LC-PFC model we have investigated the growth of PTC nucleus from the isotropic phase and the CSA phase on particle scale. An overall picture for the growth of the PTC phase is presented for shape evolution and nematic topological defect structure formation. It is demonstrated that the shape evolution for the PTC phase growth are mainly determined by crystalline anisotropy. The coupling strength exerts little influence on the shape of growing PTC nucleus. Only the shape of the PTC nucleus grown from the CSA phase also depends on the misorientation of PTC and CSA. Moreover, for the formation process of the nematic topological structure of the PTC phase, the formation of the PTC topological structure starts from nucleation of $+\frac{1}{2}$

and $-\frac{1}{2}$ disclination pairs at the PTC growth front, and leads to the coalescence of $+\frac{1}{2}$ pairs forming a hexagonal cell consisting of one $+1$ vortex surrounded by six $-\frac{1}{2}$ disclinations. The coupling strength influences the kinetics of topological defect formation, and strong coupling strength accelerates the formation of nematic topological structure. Thus, while morphological shapes of plastic crystals might look similar to that of metal systems, the dynamics of the growth process shows strong differences.

For future work, it is interesting and meaningful to extend the present study to three spatial dimensions. The topological defect formation of plastic crystal with crystal structures, such as simple cubic, body-centered crystal, face-centered crystal, etc., may provide more amazing scenarios of topological defect formation. Also, it is worth to study the plastic crystal growth with polar and non-spherical particles.

ACKNOWLEDGMENTS

This work has been supported by EU FP7, PHASE-FIELD under no.247504, German Science Foundation within SPP1296 (Grant No. Vo899/7), Nature Science Foundation of China (Grant Nos.10974228, 51071128), and 2013 DAAD-CSC postdoctoral scholarship.

Appendix A: Semi-implicit Fourier method for the LC-PFC model

A system of six coupled nonlinear partial differential equations need to be solved in the liquid crystal PFC model. In order to numerically solve this system efficiently, we decoupled and linearized it. Considering the tracelessness and symmetry of the nematic tensor as shown in equation (1), we can extract the variables $q_i \equiv Q_{i,1}$ and $q_i^\natural \equiv Q_{i,1}^\natural$, with $\mathbf{q} = (q_1, q_2)^\top$ and $\mathbf{q}^\natural = (q_1^\natural, q_2^\natural)^\top$. The dynamic equations (3) and (4) thus have the compact form

$$\begin{aligned}\dot{\psi} &= 2\alpha_1 \Delta \psi^\natural + 2\alpha_3 \blacktriangle_i q_i^\natural \\ \dot{q}_i &= 4\alpha_1 \Delta q_i^\natural - 8\alpha_4 q_i^\natural + 2\alpha_3 \blacktriangle_i \psi^\natural.\end{aligned}\quad (\text{A1})$$

The terms containing the operator \blacktriangle can be expanded, as

$$\blacktriangle_i q_i^\natural = (\partial_1 \partial_1 - \partial_2 \partial_2) q_1^\natural + 2\partial_1 \partial_2 q_2^\natural$$

and the thermodynamic conjugates read

$$\begin{aligned}\psi^\natural &= \omega_\psi(\psi, \mathbf{q}) + \overbrace{2A_1 \psi + 2A_2 (\Delta + \Delta^2) \psi}^{L_\psi^\psi(\psi)} + \overbrace{(-B_3) \blacktriangle_i q_i}^{L_\psi^q(\mathbf{q})}, \\ q_i^\natural &= \omega_q(\psi, \mathbf{q})_i + \underbrace{4D_1 q_i - 2D_2 \Delta q_i}_{L_q^q(q_i)} + \underbrace{(-B_3) \blacktriangle_i \psi}_{L_{q,i}^\psi(\psi)},\end{aligned}\quad (\text{A2})$$

with the linear parts $L_\psi^\psi(\psi), L_\psi^q(\mathbf{q}), L_q^q(q_i)$ and $L_{q,i}^\psi(\psi)$ and the polynomials

$$\begin{aligned}\omega_\psi(\psi, \mathbf{q}) &= -\psi^2 + \frac{2}{3} \psi^3 + \frac{1}{2} (2\psi - 1)(q_1^2 + q_2^2), \\ \omega_q(\psi, \mathbf{q})_i &= \psi(\psi - 1)q_i + \frac{1}{4} q_i (q_1^2 + q_2^2).\end{aligned}\quad (\text{A3})$$

We define the Fourier wave vector $\mathbf{k} = (k_1, k_2)^\top$ and introduce the Fourier transform \mathcal{F} of the order parameter fields, as

$$\psi \mapsto \mathcal{F}(\psi) =: \hat{\psi}(\mathbf{k}), \quad q_i \mapsto \mathcal{F}(q_i) =: \hat{q}_i(\mathbf{k}).$$

Thus, we can write the differential operators in Fourier space, as

$$\begin{aligned}\Delta &\rightarrow \hat{\Delta} := -(k_1^2 + k_2^2) = -|\mathbf{k}|^2 \\ \blacktriangle &\rightarrow \hat{\blacktriangle} := \begin{pmatrix} -(k_1^2 - k_2^2) \\ -k_1 k_2 \end{pmatrix}.\end{aligned}\quad (\text{A4})$$

Discretizing (A1) in time using a semi-implicit backward Euler-discretization and transforming the equation to Fourier space leads to the spectral method used in our calculations. Therefore, we transform the linear differential operators L_*^* of (A2) using the operators defined above and denote it with a hat, i.e.

$$\begin{aligned}\hat{L}_\psi^\psi[\hat{\psi}] &:= 2A_1 \hat{\psi} + 2A_2 (\hat{\Delta} + \hat{\Delta}^2) \cdot \hat{\psi} \\ &= (2A_1 + 2A_2 (-|\mathbf{k}|^2 + |\mathbf{k}|^4)) \cdot \hat{\psi}\end{aligned}\quad (\text{A5})$$

and the other operators in an analogous manner.

The nonlinear polynomials (A3) are evaluated in real space and transformed afterwards, i.e.

$$\hat{\omega}_\psi(\psi, \mathbf{q}) := \mathcal{F}(\omega_\psi(\psi, \mathbf{q})).\quad (\text{A6})$$

Therefore, in each time step the order parameters ψ and \mathbf{q} have to be transformed between real and Fourier space using efficient implementations of \mathcal{F} and \mathcal{F}^{-1} .

Let $0 = t^0 < t^1 < \dots < t^N = T$ be a discretization of a time interval $[0, T]$, with $t^{n+1} - t^n =: \tau$ the timestep width. The finite difference approximation

$$\dot{\psi} \approx \frac{\hat{\psi}^{n+1} - \hat{\psi}^n}{\tau},$$

with $\hat{\psi}^n \equiv \hat{\psi}(t^n)$ and \hat{q}_i in an analogous manner, inserted into the transformed equations, using (A5) and (A6), leads to an iterative procedure:

Let $\hat{\psi}^0 = \mathcal{F}(\psi^0)$, $\hat{\mathbf{q}}^0 = \mathcal{F}(\mathbf{q}^0)$. For $n = 0, 1, 2, \dots, N$

1. solve

$$\begin{aligned}& \left(1 - \tau \left[2\alpha_1 \hat{\Delta} \cdot \hat{L}_\psi^\psi + 2\alpha_3 \hat{\blacktriangle}_i \cdot \hat{L}_{q,i}^\psi \right]\right) \hat{\psi}^{n+1} \\ &= \left(\hat{\psi}^n + \tau \left[2\alpha_1 \hat{\Delta} \cdot (\hat{L}_\psi^q[\hat{\mathbf{q}}^n] + \hat{\omega}_\psi(\psi^n, \mathbf{q}^n)) \right. \right. \\ & \quad \left. \left. + 2\alpha_3 \hat{\blacktriangle}_i \cdot (\hat{L}_q^q[\hat{q}_i^n] + \hat{\omega}_q(\psi^n, \mathbf{q}^n)_i) \right] \right),\end{aligned}\quad (\text{A7})$$

2. transform to real space:

$$\psi^{n+1} = \mathcal{F}^{-1}(\hat{\psi}^{n+1}),$$

3. for $i = 1, 2$ solve

$$\begin{aligned} & \left(1 - \tau \left[(4\alpha_1 \hat{\Delta} - 8\alpha_4) \cdot \hat{L}_q^q \right] \hat{q}_i^{n+1} \right. \\ & \quad \left. - \tau \cdot 2\alpha_3 \hat{\mathbf{A}}_i \cdot \hat{L}_\psi^q[\hat{\mathbf{q}}_i^{n,n+1}] \right) \\ = & \left(\hat{q}_i^n + \tau \left[(4\alpha_1 \hat{\Delta} - 8\alpha_4) \cdot (\hat{L}_{q,i}^\psi[\hat{\psi}^{n+1}] + \hat{\omega}_q(\psi^{n+1}, \mathbf{q}^n)_i) \right. \right. \\ & \quad \left. \left. + 2\alpha_3 \hat{\mathbf{A}}_i \cdot (\hat{L}_\psi^\psi[\hat{\psi}^{n+1}] + \hat{\omega}_\psi(\psi^{n+1}, \mathbf{q}^n)) \right] \right), \quad (\text{A8}) \end{aligned}$$

where $\hat{\mathbf{q}}_{(i)}^{n,n+1}$ are intermediate vectors defined as

$$\hat{\mathbf{q}}_{(1)}^{n,n+1} := \begin{pmatrix} \hat{q}_1^{n+1} \\ \hat{q}_2^n \end{pmatrix}, \quad \hat{\mathbf{q}}_{(2)}^{n,n+1} := \begin{pmatrix} \hat{q}_1^n \\ \hat{q}_2^{n+1} \end{pmatrix},$$

4. transform to real space:

$$q_i^{n+1} = \mathcal{F}^{-1}(\hat{q}_i^{n+1}), \quad i = 1, 2.$$

In equation (A8) the updated values ψ^{n+1} and $\hat{\psi}^{n+1}$ can be used.

-
- [1] K. R. Elder, M. Katakowski, M. Haataja, and M. Grant, Phys. Rev. Lett. **88**, 245701 (2002).
- [2] K. R. Elder and M. Grant, Phys. Rev. E **70**, 051605 (2004).
- [3] H. Emmerich, H. Löwen, R. Wittkowski, T. Gruhn, G. I. Tóth, G. Tegze, and L. Gránásy, Advances in Physics **61**, 665 (2012).
- [4] G. Tegze, L. Gránásy, G. I. Tóth, J. F. Douglas, and T. Pusztai, Soft Matter **7**, 1789 (2011).
- [5] S. Tang, Z. J. Wang, Y. L. Guo, J. C. Wang, Y. M. Yu, and Y. H. Zhou, Acta Mater. **60**, 5501 (2012).
- [6] S. Tang, R. Backofen, J. Wang, Y. Zhou, A. Voigt, and Y. M. Yu, J. Cryst. Growth **334**, 146 (2011).
- [7] Y. M. Yu, R. Backofen, and A. Voigt, J. Cryst. Growth **318**, 18 (2011).
- [8] H. Löwen, J. Phys.: Condens. Matter **22**, 364105 (2010).
- [9] E. B. Mock and C. F. Zukoski, Langmuir **23**, 8760 (2007).
- [10] A. F. Demirörs, P. M. Johnson, C. M. van Kats, A. V. Blaaderen, and A. Imhof, Langmuir **26**, 14466 (2010).
- [11] I. D. Hosein, B. S. John, S. H. Lee, F. A. Escobedo, and C. M. Liddell, J. Mater. Chem. **19**, 344 (2009).
- [12] R. Rey, J. Phys. Chem. B **112**, 344 (2008).
- [13] A. V. Tkachenko and Y. Rabin, Phys. Rev. E **55**, 778 (1997).
- [14] C. V. Achim, R. Wittkowski, and H. Löwen, Phys. Rev. E **83**, 061712 (2011).
- [15] S. Praetorius, A. Voigt, R. Wittkowski, and H. Löwen, Phys. Rev. E **87**, 052406 (2013).
- [16] E. R. Rubinstein and M. E. Glicksman, J. Cryst. Growth **112**, 84 (1991).
- [17] P. Oswald and P. Pieranski, *Smectic and Columnar Liquid Crystals* (Taylor and Francis, New York, 2006).
- [18] N. D. Mermin, Rev. Mod. Phys. **51**, 591 (1979).
- [19] G. P. Alexander, B. G. g. Chen, E. A. Matsumoto, and R. D. Kamien, Rev. Mod. Phys. **84**, 497 (2012).
- [20] P. Cremer, M. Marechal, and H. Löwen, Europhys. Lett. **99**, 38005 (2012).
- [21] R. Wittkowski, H. Löwen, and H. R. Brand, Phys. Rev. E **83**, 061706 (2011).
- [22] R. Wittkowski, H. Löwen, and H. R. Brand, Phys. Rev. E **84**, 041708 (2011).
- [23] R. Backofen and A. Voigt, J. Phys.: Condens. Matter. **21**, 464109 (2009).
- [24] S. V. Khare, S. Kodambaka, D. D. Johnson, I. Petrov, and J. E. Greene, Surf. Sci. **1-3**, 522 (2003).
- [25] T. Lopez-Leon, M. A. Bates, and A. Fernandez-Nieves, Phys. Rev. E **86**, 030702 (R) (2012).